Hypersonic laser-plasma expansion measurements with cyanide spectroscopy

CHRISTOPHER M. HELSTERN[1], CHRISTIAN G. PARIGGER[1*], BENJAMIN S. JORDAN[2],

DAVID M. SURMICK[3], ROBERT SPLINTER[4]

[1]*Physics and Astronomy Department, University of Tennessee, University of Tennessee Space Institute, Center for Laser Applications,411 B.H. Goethert Parkway, Tullahoma, TN 37388-9700, USA*
[2]*Nuclear Engineering Department, University of Tennessee, Tickle College of Engineering, 1412 Circle Drive, Knoxville, TN 37912, USA*
[3]*Physics and Applied Physics, University of Massachusetts Lowell, Lowell, MA 01854, USA*
[4]*Welling Medical, Van der Waals Park 22, 9351 VC Leek, The Netherlands*
Corresponding author E-mail: cparigge@tennessee.edu (C.G. Parigger)

ABSTRACT: This article reports new measurements of laser-induced plasma hypersonic expansion measurements of diatomic molecular cyanide (CN). Focused, high-peak power 1064-nm Q-switched radiation of the order of 1 TW/cm^2 generates optical breakdown plasma in a cell at pressures of 1.1 and 2.8×10^5 Pascal. Line-of-sight (LOS) analysis of recorded molecular spectra indicate the outgoing shockwave at expansion speeds well in excess of Mach number 5. Spectra of atomic carbon confirm an increased electron density near the shock wave, and equally, molecular CN spectra reveal higher excitation temperature near the shockwave. The results are consistent with corresponding high-speed shadowgraphs obtained by visualization with an effective shutter speed of 5 nanosecond. In addition, LOS analysis and application of integral inversion techniques allow inferences about the spatio-temporal distribution of the plasma.

PACS Codes: 52.70.-m, 33.20.-t, 52.25.Jm, 42.62.Fi

Keywords: Plasma diagnostics, molecular spectra, plasma spectroscopy, laser spectroscopy, laser-induced breakdown spectroscopy.

1. INTRODUCTION

Molecular recombination spectra are readily measured following optical breakdown in gases, the cyanide (CN) molecule can be recognized rather early for time delays of the order of 100 ns after cessation of the laser pulse [1]. Gas mixtures are selected for the purpose of measuring CN spatio-temporal distributions associated with high-speed, hypersonic gas-dynamic expansion. Applications of cyanide spectroscopy include various scientific areas including medical research and selected engineering endeavors.

Cyanides are connected to many living organisms and are created through man-made processes, but they are highly toxic. Human exposures can occur through accidental ingestion or inhalation of cyanides. Synthetic materials can be found in 21st century buildings and furnishings which produce toxic combustion byproducts, like hydrogen cyanide (HCN), when burned [2]. Victims of these fires can have significant intakes of HCN, which can lead to cyanide poisoning and ultimately death. Cyanide detection can identify cyanide poisoning occurrences in humans and can assist in determination of adequate treatment. Additionally, HCN can be produced by bacteria such as Pseudomonas aeruginosa [3]. Immune-compromised patients such as those with cystic fibrosis (CF) are susceptible to increased morbidity and mortality when afflicted by these bacteria [3]. Detection of bacterial produced HCN in the airways will lead to earlier treatment of immune-compromised infected with these bacteria.

The diatomic molecule CN has remained a target for improved detection capability and deeper understanding largely because engineers cannot replicate CN's effectiveness for certain industrial applications with any other compound. For example, 90% of the gold mining operations world-wide utilize CN because of its availability, effectiveness, and cost efficiency [4]. Although accidents, injuries, and environmental mishaps are possible, when they occur, they require specialized detection capability to ensure safety of the workers during the remediation.

The engineering applications associated with plastic manufacturing that continue to use cyanide create a downstream problem for firefighters, analogous to that of fire victims mentioned above. Fire fighters must go into buildings where the plastics that may have used cyanide during their manufacture are now evolving their constituents into the air as they are consumed by fire [5]. Again, detection and assessment of amount of CN present is needed to help keep fire fighters safe.

Engineers continue to look for a means of obtaining the CN properties that customers need, but that do not have the potential health hazards that are present with CN. Engineers have been seeking ways to lower the cyanide utilization in the nitriles chemical industry [6]. Alternatives to cyanide are also being sought for the mining industry, but this task has proven difficult because the replacement candidates are often not as broadly applicable and must be tailored to the specific ore [7].

In addition, CN is a component of vehicle exhaust [8]. It is important for engineers to continue to research the details of CN detection and evaluation to be able to characterize the relative emission impacts that different vehicles contribute [9]. There is CN production potential in other combustion processes as well and continued understanding of what CN production should be expected is going to continue to drive interest and investigation into CN even if engineers are able to replace CN in many industrial applications [10].

2. EXPERIMENTAL DETAILS

The standard experimental components are used for laser-induced breakdown spectroscopy and have been summarized previously, e.g., see Ref. [1], but are included for completeness. The experimental arrangement consists of a set of components typical for time-resolved, laser-induced optical emission spectroscopy, or nanosecond laser-induced breakdown spectroscopy (LIBS) [11]. Primary instrumentation includes a Q-switched Nd:YAG device (Quantel model Q-smart 850) operated at the fundamental wavelength of 1064-nm to produce full-width-at-half-maximum 6-ns laser radiation with an energy of 850 mJ per pulse, a laboratory type Czerny-Turner spectrometer (Jobin Yvon model HR 640) with a 0.64 m focal length and equipped with a 1200 grooves/mm grating, an intensified charge coupled device (Andor Technology model iStar DH334T-25U-03) for recording of temporally and spatially resolved spectral data, a laboratory chamber or cell with inlet and outlet ports together with a vacuum system, electronic components for synchronization, and various optical elements for beam shaping, steering and focusing.

For the generation of optical breakdown micro-plasma, a singlet lens (Thorlabs model LA1509-C) is used close to the top entrance window of one arm of the chamber containing the 1:1 $CO_2:N_2$ atmospheric gas mixture (Airgas ultra-high purity N_2 and research grade CO_2). For 1:1 imaging of the plasma onto the 100 µm spectrometer slit, a fused silica plano-convex lens (Thorlabs model LA4545) is employed. For the CN experiments reported here, the laser pulse energy is attenuated with beamsplitters and apertures from 850 to 170 mJ/pulse. Measurements are performed with and without an Order Sorting Filter (Oriel model 51250) with a cut-on wavelength of 309 nm and transmittance range of 325 nm to evaluate the CI 193.09 nm atomic carbon line in second order interference as identifed in previous work [1].

In previous experiments, captured shadowgraphs of the breakdown plasma [12] served the purpose of visualizing the plasma expansion when using 850 mJ, 6-ns radiation. However, it is important to obtain shadowgraphs for plasma excitation energies that were employed for time-resolved spectroscopy. Shadowgraphs reported in this work are captured using two separate laser devices (Continuum Surelite model SL I-10) that can be externally operated to deliver laser pulses with a well-defined time delay showing less than ± 1 ns trigger-jitter between the pulses. For visualization studies, both lasers are frequency-doubled to operate at the 2nd harmonic, 532-nm wavelength, and both beams are spatially overlapped. Both pulses can be delivered with a minimum time delay of 300 ns. Shadowgraphs

are recorded by external synchronization of the Surelite and Quantel laser devices and by external triggering the camera (Silicon Video 9C10 color camera) that records the images that are projected onto a screen.

Two typical images are reported here. First, Figure 1 displays a shadowgraph of the IR, 1064-nm laser-induced plasma for an excitation energy of 170 mJ, 6-ns pulse width. The shadowgraph is captured using a single, 5-ns pulse-width 532-nm beam. The expanding shock-wave is clearly visible, including the central plasma kernel. The image is nearly spherical, previously reported shadowgraphs that utilize 850-mJ excitation would reveal stronger deviation from spherical symmetry than the images obtained with 170 mJ/pulse. The expanding shockwave radius is consistent with previous assessments of hypersonic laser-plasma expansion images [12] that employ the Taylor-Sedov energy$^{1/5}$ dependency [13]. Tables 1 and 2 compare energies of 160 mJ and 200 mJ, respectively, computed blastwave radii for standard ambient temperature and pressure (SATP) air and the CN mixture. Consequently, measured shadowgraphs in air provide an excellent guide for the gaseous mixture.

Table 1: Computed shockwave radii for SATP air and for the molar CN mixture, 160 mJ.

time delay (ns)	r (mm) for air [ρ = 1.2 kg/m³]	r (mm) for CN mix [ρ = 1.63 kg/m³]
200	1.40	1.31
450	1.93	1.82
700	2.31	2.17
950	2.61	2.45
1200	2.86	2.69
1450	3.09	2.90

Table 2: Computed shockwave radii for SATP air and for the molar CN mixture, 200 mJ.

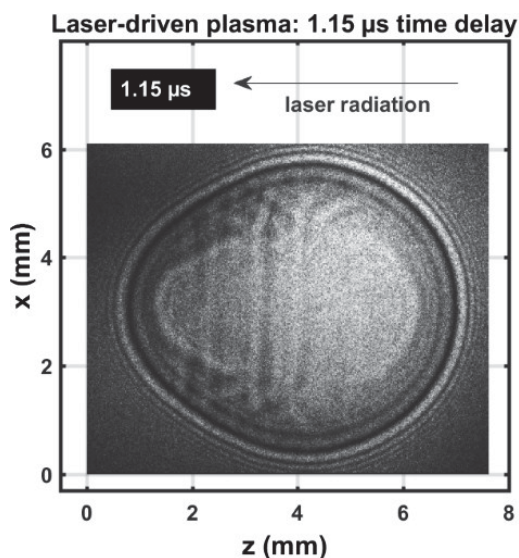| time delay (ns)	r (mm) for air [ρ = 1.2 kg/m³]	r (mm) for CN mix [ρ = 1.63 kg/m³]
200	1.46	1.37
450	2.02	1.90
700	2.41	2.27
950	2.73	2.56
1200	2.99	2.81
1450	3.23	3.04

Figure 1: Single-shot shadowgraph of the expanding laser-induced plasma intiated with a 170-mJ, 6-ns, 1064-nm focused beam, and imaged using a 5-ns, 532-nm backlight time-delayed by 1.15 μs ± 0.05 μs.

And second, Figure 2 exhibits composite shadowgraphs obtained by initiating laser-plasma with the first, green, 90 mJ/pulse, 5-ns beam, and subsequently, initiating laser plasma at the shockwave with the second, green, 110 mJ/pulse, 5-ns beam that exactly overlaps spatially, but is time delayed by 0.45 µs. The composite image is obtained by the 0.45 µs time delay and an extra 30-ns optical time delay for each beam. The initial, elongated multiple-breakdown in the central region is imaged with the first 5-ns pulse-width beam. The near-spherical shockwave is imaged with the second 5-ns pulse-width beam and the corresponding 30-ns time delayed beam. However, the second beam initiates breakdown at the forward side (left in the image) and at the side of the incoming beam (right in the image) indicated by a dark ring – the extent of that dark ring is due to the use of a 5-ns pulse-width beam, time-delayed by 30 ns for shadowgraph capture of expansion dynamics. The expansion speed of the second optical breakdown at the right of the image is well over one order of magnitude larger than hypersonic speed in SATP air.
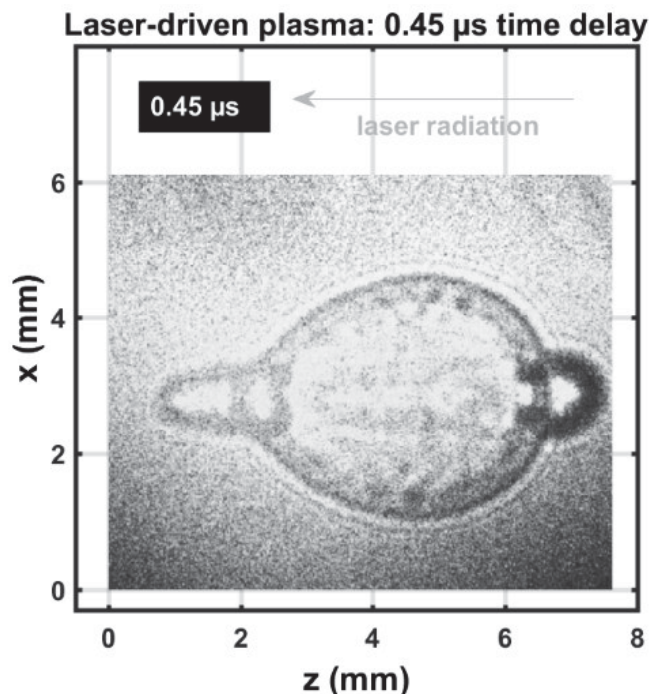

Figure 2: Single-shot shadowgraph of laser-induced plasma initiated with 90-mJ and 110-mJ, 5-ns, 532-nm focused beams, and imaged using two 5-ns, 532-nm backlights time-delayed by 0.03 µs, 0.45 µs, and 0.48 µs.

3. RESULTS AND DISCUSSION

The experimental series for the measurement of the CN molecular distribution after optical breakdown includes evacuating the cell to a nominal backing pump pressure of the order of 1 Pa (10^{-2} Torr), followed by generating the mixture from ultra-high pure N_2 and research grade CO_2. Optical breakdown was generated inside the chamber at a rate of 10 Hz, with the laser beam focused with f/5 optics from the top, or parallel to the slit. The detector pixels are binned in 4-pixel tracks along the slit direction, resulting in obtaining 256 spectra for each time delay. Recording of measurements with and without the Order Sorting filter consist of 100 accumulations collected for 21 time delays at 250 ns steps. These runs allow for evaluation of CN plasma spatial and temporal characteristics and the CI 193.09 nm atomic carbon line in second order. Figures 3 and 4 illustrate recorded spatio-temporal spectra that were recorded along the line-of-sight and are accumulated over 100 individual laser-plasma events. The slit-height corresponds to the z-direction and the line-of-sight corresponds to the y-direction in reference to Figures 1 and 2.
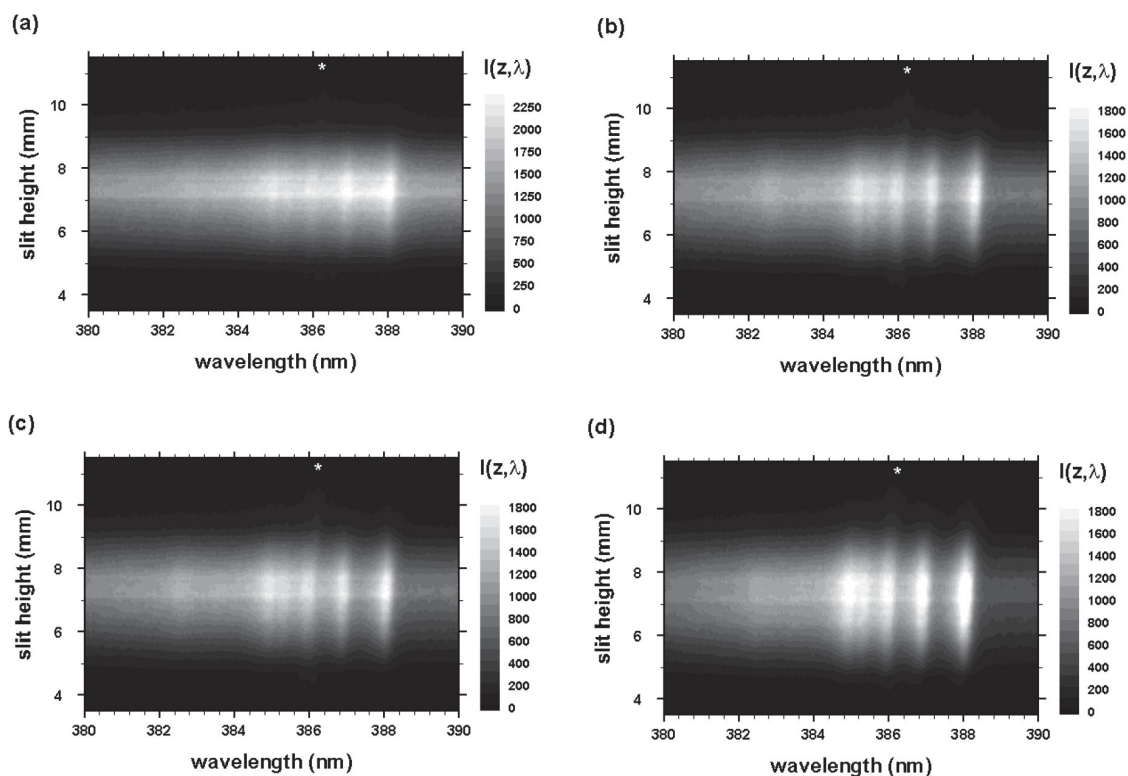
Figure 3: Optical brekdown CN-spectra in a 1:1 molar CO_2:N_2 atmospheric gas mixture for time delays (a) 200 ns, (b) 450 ns, (c) 700 ns, and (d) 950 ns. Spectrometer-detector gatewidth: 125 ns. The asterisk, * , indicates the 2nd order, neutral carbon line.
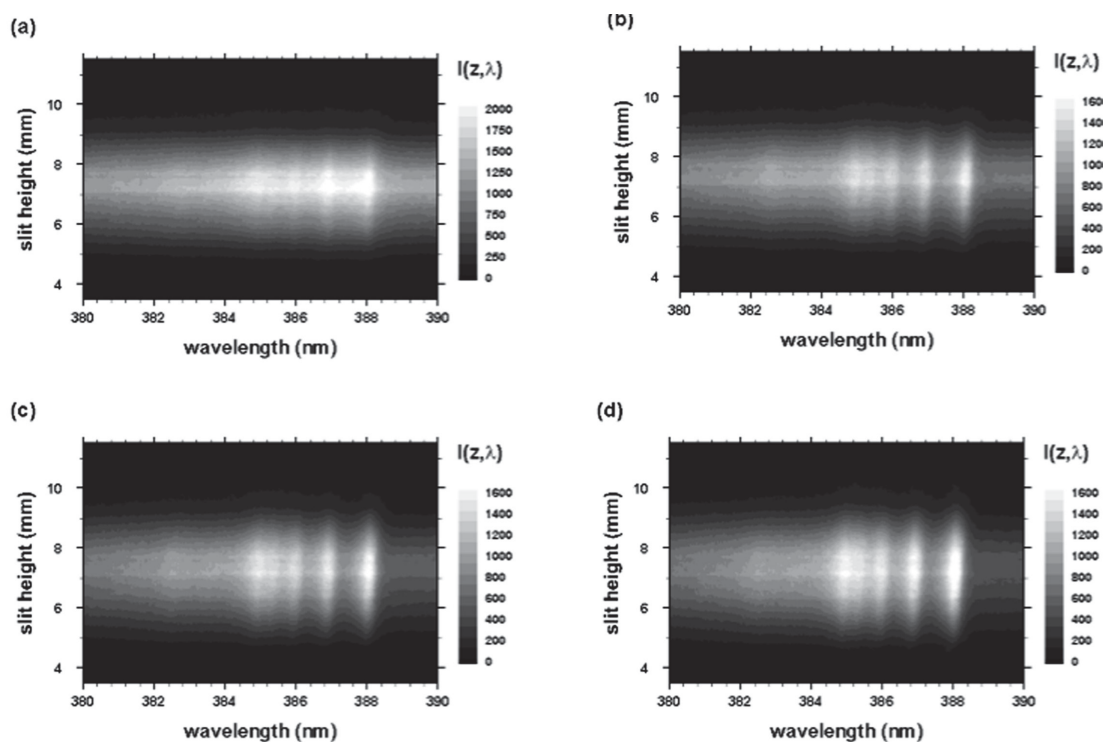

Figure 4: Optical brekdown CN-spectra as in Fig. 3 for time delays (a) 200 ns, (b) 450 ns, (c) 700 ns, and (d) 950 ns, but recorded with a 309-nm cut-on wavelength filter.

Figure 5 exhibits results of the analysis of the filtered, line-of-sight molecular CN-spectra. The figures reveal the occurrence of the outgoing shockwave along with temperature variations in the central region of the plasma. These data of slit-height vs. temperature show increased temperature near the edges.
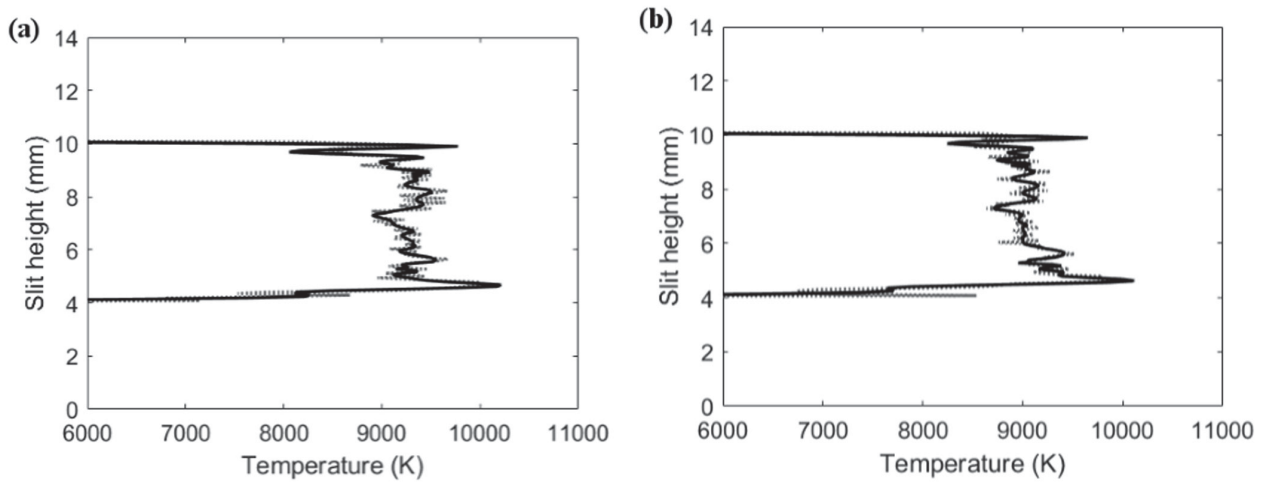

Figure 5: Temperature vs. slit height for filtered CN-spectra (a) 700-ns and (b) 950-ns time delay.

Unfiltered spectra contain an overlap of the CI 193.09-nm atomic carbon line in second order and the 2-2 CN band head of 386.19 nm, where filtered spectra only contain the 2-2 CN band head of 386.19 nm. CI 193.09-nm atomic carbon line in second order Stark widths were evaluated for filtered and unfiltered spectra using peak fitting programs. The difference between the filtered and unfiltered spectra is obtained by applying deconvolution. Figure 6 illustrates the results for the widths at full-width-half maximum of the peak. Figure 6 reveals that larger Stark widths are seen near the edges of the plasma, while smaller Stark widths are near the center of the plasma.
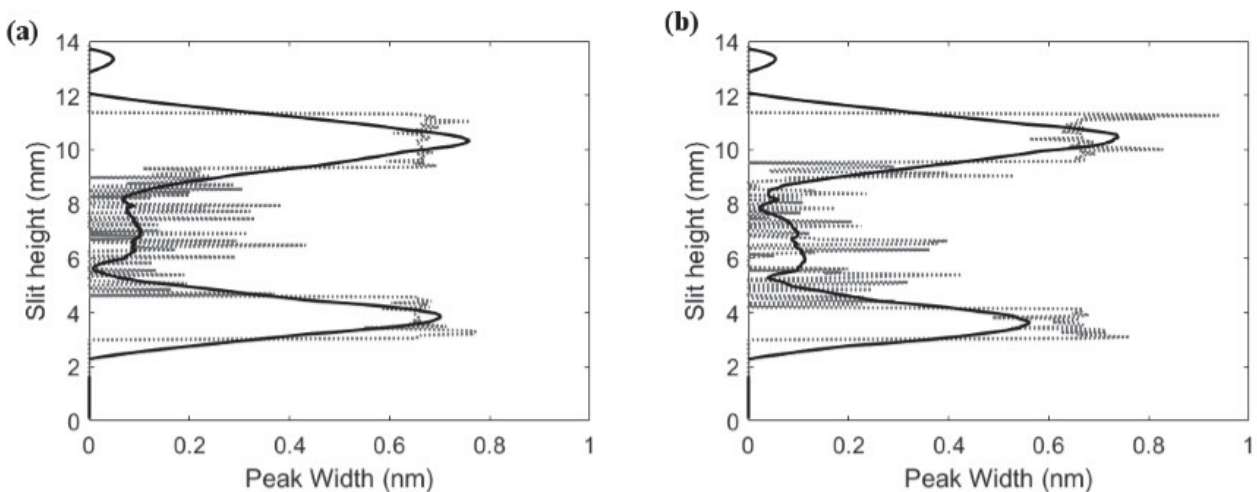

Figure 6: Inferred widths of CI 193.09-nm atomic carbon line in second-order vs. slit height for time delays of (a) 700 ns and (b) 950 ns.

The electron number density, n_e, can be determined from the Stark full-width at half maxiumum, $\Delta\lambda_{Stark}$, of the CI 193.09-nm atomic carbon line [14] measured in 2nd order,

$$\Delta\lambda_{Stark} = 2w \, n_e \left(10^{17} cm^{-3}\right),$$ (1)

where the width parameter, w, is extrapolated [14, 15] to amount to $w \approx 0.0029$ nm. Figure 7 displays the calculated electron densities versus slit height. The calculated electron densities are of the order of $n_e \sim 10^{17}$ cm^{-3} in the central

region. Higher electron desnsities are seen near the edges of the plasma, while smaller electron densities are near the center of the plasma.

Using the Taylor-Sedov Blast wave model [11, 12] the radius of the plasma, R, at time delay of 450 ns is ~ 1.9 mm which would indicate higher electron density near the shockwave, which is consistent with the results shown in Figure 7.
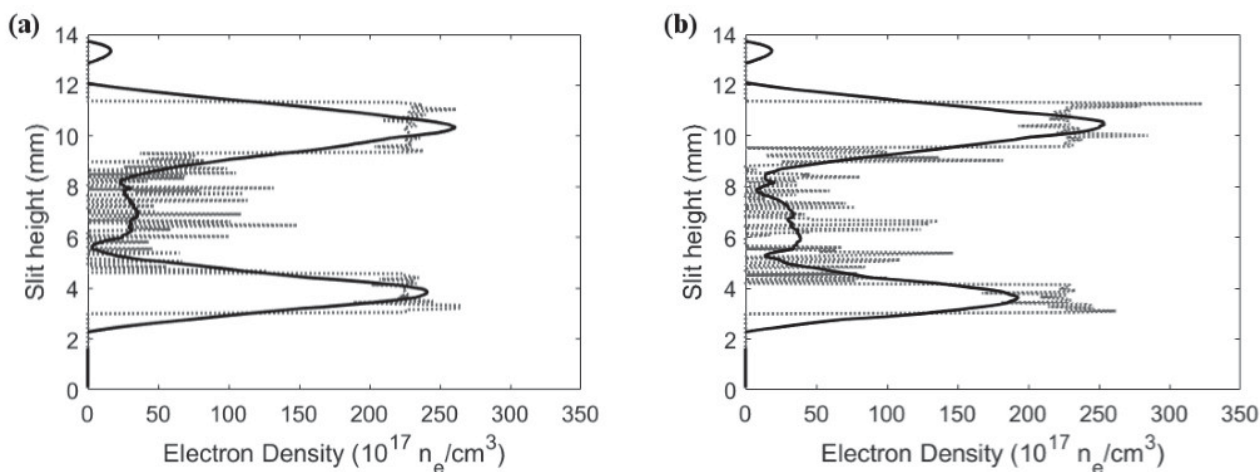

Figure 7: Calculated electron densities versus slit height for time delays of (a) 700 ns and (b) 950 ns.

In view of the shadowgraphs that are recorded in the 0.5 to 1 μs range (see Figs. 1 and 2) it would be acceptable to apply an Abel inverse tranfrom. Deviation from spherical symmetry is minimal for time delays of the order of 1 μs provided laser-induced excitation is accomplished with IR radiation of the order of 200 mJ/pulse or less. The analysis of the molecular CN spectra follows the same symmetrization methods as applied for atomic hydrogen spectra [16, 17]. The use of Chebyshev polynomials for the inversion of the integral equation,

$$I(z,\lambda) = 2 \int_z^\rho \varepsilon(r,\lambda) \frac{r}{\sqrt{r^2 - z^2}} \, dr \,,$$
(2)

allows one to directly invert measured data. The z-direction corresponds to the slit-height, and the line-of-sight integration is along the y-direction in view of Figure 1. The choice of the number of here 15 polynomials for the inversion [18, 19] maintains fidelity of the spectra and is equivalent to the use of a digital filter resulting in broadening of the computed radial spectra. A smaller number of polynomials would cause smaller spectral resolution. The measured, line-of sight data, $I(z,\lambda)$, along the slit dimension, z, are inverted for each wavelength, λ, to obtain the radial intensity distribution, $\varepsilon(r,\lambda)$, with the upper limit much larger, $\rho \gg R$, than the radius, R, of the plasma.

The radial spectra are computed from the 2-dimensional line-of-sight data (see Figs. 3 and 4) that were accumulated with an intensified camera attached to the spectrometer that allows one to resolve spectra along the slit. The recorded data are calibrated, corrected for the system sensitivity using standard lamps, and prepared for Abel inversion. Usually, when recording 2-D spectra, slight wavelength variations towards the edges of the slit occur, but these variations have been taken care of in preparing the data for Abel inversion. Figures 8 and 9 illustrate computed Abel inverted spectra. Only subtle differences may be recognizable near the 2-2 CN band edge due to the CI line when comparing Figs. 8 and 9, however, Fig. 8 also contains electron-density information that confirms higher electron density near the edges than the central regions, and consequently, higher electron temperature for adiabatic expansion.
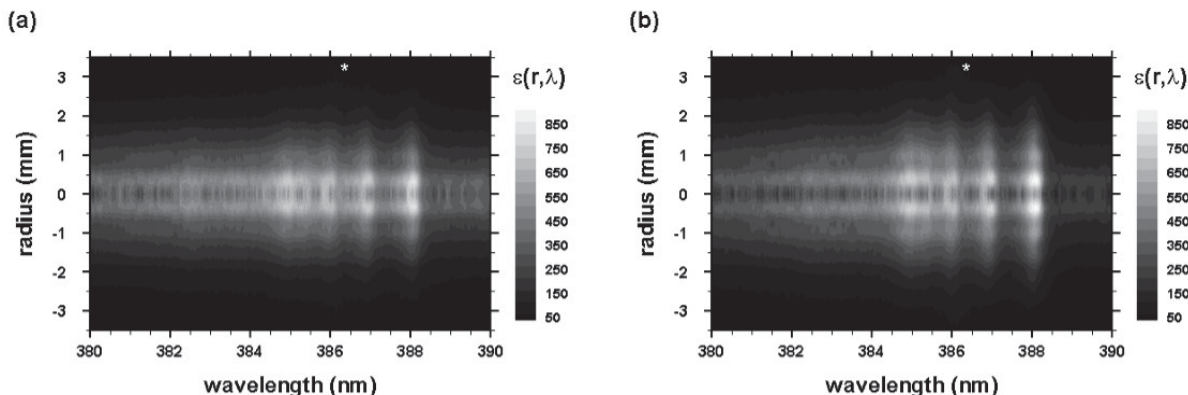
Figure 8: Abel inverted data of Figure 3 for time delays of (a) 450 ns and (b) 950 ns. The asterisk, * , indicates the 2nd order, neutral carbon line.
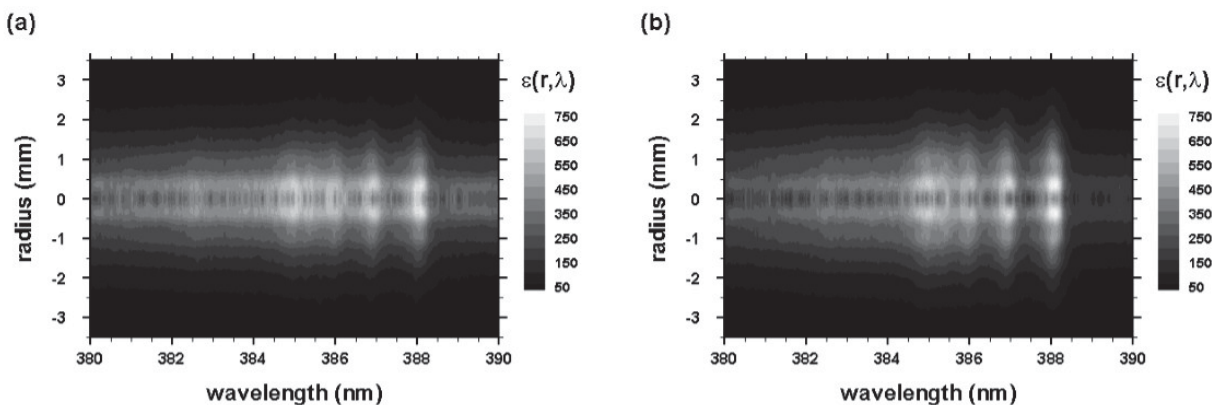

Figure 9: Abel inverted data of Figure 4 for time delays of (a) 450 ns and (b) 950 ns.

Both line-of-sight and Abel inverted data sets of the CN-spectra are subjected to analysis with the so-called NMT, or Nelder-Mead temperature, program that has been made available along with the required CN-violet system data set [20, 21]. Figure 10 exhibits a typical CN-spectrum and fit of line-of-sight data accomplished in this work. Analysis of the Abel-inverted data is expected to reveal similar results for the shockwave, however, in view of the shadowgraphs in Figs. 1 and 2, variations of the CN distribution inside the shockwave and inside the plasma kernel are anticipated.
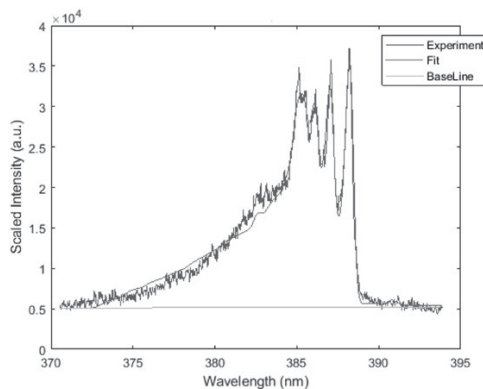

Figure 10: Typical fitted CN spectrum, T = 8947 K, fit FWHM = 0.47 nm.

4. CONCLUSIONS

Laser-plasma expansion following optical breakdown occurs at well above hypersonic speed. Measurements of recombination CN-spectra within the first few microseconds yields results as expected from atomic hydrogen, Balmer series laser spectroscopy. The analysis reveals higher electron and higher CN-excitation temperature near the shockwave than in the central region for time delays of the order of one microsecond. The expansion characteristics are deduced from a systematic analysis of the recorded line-of-sight spectra. Application of Abel inversion is reasonable and supported by shadowgraphs recorded in SATP air for laser-plasma initiation for similar energy/pulse as utilized for measurements of molecular spectra.

References

[1] C.G. Parigger, C.M. Helstern, G. Gautam, *Int. Rev. At. Mol. Phys.* **8** (2017) 25.

[2] K.W. Fent, D.E. Evans, K. Babik, C. Striley, S. Bertke, S. Kerber, D. Smith, G.P. Horn, *J. Occup. Environ. Hyg.* **15** (2018) 399.

[3] D.D. Arslanov, M.P.P. Castro, N.A. Creemers, A.H. Neerincx, M. Spunei, J. Mandon, S.M. Cristescu, P. Merkus, F.J.M. Harren, *J. Biomed. Opt.* **18** (2013) 107002.

[4] T.I. Mudder, M.M. Botz, *Eur. J. Miner. Process. Environ. Protect.* **4** (2004) 62.

[5] D.M. Bolstad-Johnson, J.L. Burgess, C.D. Crutchfield, S. Storment, R. Gerkin, J.R. Wilson, *Am. Ind. Hyg. Assoc. 61* (2000) 636.

[6] C. Plass, A. Hinzmann, M. Terhorst, W. Brauer, K. Oike, H. Yavuzer, Y. Asano, A. Vorholt, T. Betke, H. Gröger, *Am. Chem. Soc. Catal.* **9** (2019) 5198.

[7] G. Hilson, A.J. Monhemius, *J. Clean. Prod.* **14** (2006) 1158.

[8] S.G. Moussa, A. Leithead, S-M Li, T.W. Chan, J.J.B. Wentzell, C. Stroud, J. Zhang, P. Lee, G.L. Jeffery, R.Brook, K. Hayden, J. Narayan, J. Liggio, *Atmos. Environ.* **131** (2016) 185.

[9] M.M. Baum, J.A. Moss, S H. Pastel, G.A. Poskrebyshev, *Environ. Sci. Technol.* **41** (2007) 857.

[10] P. Dagaut, P. Glarborg, M.U. Alzueta, *Prog. Energ. Combust.* 34 (2008) 1.

[11] D.A. Cremers, L.J. Radziemski, *Handbook of Laser-Induced Breakdown Spectroscopy*, John Wiley & Sons Ltd, USA, 2006.

[12] G. Gautam, C.M. Helstern, K.A. Drake, C.G. Parigger, *Int. Rev. At. Mol. Phys.* **7** (2016) 45.

[13] G.I. Taylor, *Proc. Roy. Soc. A* **201** (1950) 175.

[14] M. Dackman, Laser-Induced Breakdown Spectroscopy for Analysis of High-Density Methane-Oxygen Mixtures, Master's Thesis, University of Tennessee, Knoxville, TN, 2014.

[15] H.R. Griem, *Spectral Line Broadening by Plasmas,* Academic Press, New York, USA, 1974.

[16] C.G. Parigger, G. Gautam, D.M. Surmick, *Int. Rev. At. Mol. Phys.* **6** (2015) 43.

[17] C.G. Parigger, D.M. Surmick, G. Gautam, *J. Phys.: Conf. Ser.* **810** (2017) 012012.

[18] G. Pretzler, *Z. Naturforsch.* **46a** (1991) 639–641.

[19] G. Pretzler, H. Jäger, T. Neger, H. Philipp, and J. Woisetschläger, *Z. Naturforsch.* **47a** (1992) 955.

[20] C.G.Parigger, A.C.Woods, D.M.Surmick, G. Gautam, M.J.Witte, J.O.Hornkohl, *Spectrochim. Acta Part B* **107** (2015) 132.

[21] C.G. Parigger, J.O. Hornkohl, Quantum Mechanics of the Diatomic Molecule with Applications, IOP Publishing, Bristol, UK, 2019.